

## The dynamics of NAO teleconnection pattern growth and decay

By STEVEN B. FELDSTEIN\*

*The Pennsylvania State University, USA*

(Received 1 March 2002; revised 19 August 2002)

### SUMMARY

This investigation performs both diagnostic analyses with NCEP/NCAR re-analysis data and forced, barotropic model calculations to examine the dynamical mechanisms associated with the growth and decay of the North Atlantic Oscillation (NAO) teleconnection pattern. The diagnostic calculations include projection and composite analyses of each term in the stream-function-tendency equation.

The results of the analyses reveal a complete life cycle of growth and decay within approximately two weeks. The positive NAO phase is found to develop after anomalous wavetrain propagation across the North Pacific to the east coast of North America. This contrasts with the negative NAO phase which appeared to develop *in situ*.

Both high-frequency (period < 10 days) and low-frequency (period > 10 days) transient eddy fluxes drive the NAO growth. After the NAO anomaly attains its maximum amplitude, the high-frequency transient eddy fluxes continue to drive the NAO anomaly in a manner that is consistent with a positive feedback process. The decay of the NAO occurs through both the divergence term and the low-frequency transient eddy fluxes. The temporal and spatial properties of the divergence term are found to be consistent with Ekman pumping. These results illustrate many important differences between the NAO and Pacific/North American (PNA) teleconnection patterns, perhaps most striking being that the NAO life cycle is dominated by nonlinear processes, whereas the PNA evolution is primarily linear. In addition, the relation between the NAO and the zonal index is discussed.

KEYWORDS: Intraseasonal variability Zonal index

### 1. INTRODUCTION

The subject of atmospheric teleconnection patterns has stimulated much research over the past 70 years. This era of teleconnection pattern research began with the extensive and thorough analysis of Walker and Bliss (1932). Numerous studies have been published since that time, including such prominent papers as those by van Loon and Rogers (1978) and Hurrell (1995). Most investigations now find that there are two dominant modes of variability in the northern hemisphere during the winter season, the so-called North Atlantic Oscillation (NAO) and Pacific/North American (PNA) teleconnection patterns. For both patterns this dominance extends from weekly (Feldstein 2000) to interannual time-scales (e.g. Barnston and Livezey 1987; Kushnir and Wallace 1989). Several recent papers have shown that on intraseasonal time-scales the NAO is closely linked to the dominant pattern of zonal mean flow variability. For example, DeWeaver and Nigam (2000a) find a linear correlation of 0.80 between the principal component time series of the NAO and that of the first empirical orthogonal function of the zonal mean zonal wind (this zonal mean pattern is usually referred to as the zonal index (ZI)).

\* Corresponding address: EMS Environment Institute, The Pennsylvania State University, University Park, PA 16802, USA. e-mail: sbf@essc.psu.edu

Several recent investigations have examined the dynamic processes which drive ZI anomalies\* (Robinson 1991, 1996, 2000; Yu and Hartmann 1993; Feldstein and Lee 1996, 1998; Lee and Feldstein 1996; Lorenz and Hartmann 2001) on intraseasonal time-scales. Feldstein and Lee (1998) and Lorenz and Hartmann (2001) find that the ZI completes its life cycle of growth and decay within a time span of approximately two weeks. The key results of both of these studies suggest a simple dynamical picture in which the growth of the ZI is driven by transient, eddy momentum fluxes, and that the decay of the ZI is through frictional dissipation. Furthermore, these studies also suggest that high-frequency (period  $< 10$  days) transient eddy momentum fluxes prolong the ZI life cycle in a manner consistent with an eddy feedback process. This picture describes the ZI both for the winter and summer seasons of the southern hemisphere and for the northern hemisphere summer. However, for the ZI during the northern hemisphere winter, this picture is complicated by the large role played by the interaction between the transient eddies† and the climatological stationary eddies (Feldstein and Lee 1998; DeWeaver and Nigam 2000a, 2000b).

The focus of the present study is to investigate the dynamical processes that are associated with the life cycle of the NAO teleconnection pattern on intraseasonal time-scales. Given the large correlation between the NAO and the ZI during the northern hemisphere winter, it is anticipated that the NAO will exhibit many similarities in the dynamics of its life cycle to that for the ZI. As followed by Feldstein (1998a, 2002), the main approach will be to examine closely the temporal evolution of each term in the stream-function-tendency equation (the inverse Laplacian of the vorticity equation) during the NAO life cycle. For this investigation, I will concentrate on the dynamics at the 300 mb pressure surface. I choose this level for two reasons. Firstly, as shown later, high-frequency transient eddy fluxes play an important role in driving the NAO. Since these eddies are confined to the troposphere (Charney and Drazin 1961), the key dynamical processes that drive the NAO must also be within the troposphere. Secondly, since the amplitude of the NAO increases with height in the troposphere, a pressure level in the upper troposphere is selected, in order to examine the NAO in a region where its signal is largest. As we will find, the above approach will help us to identify the dominant dynamical processes during different stages of the NAO life cycle.

In section 2, the data and diagnostic techniques are presented. This is followed in sections 3 and 4 with examinations of the spatial structure and temporal evolution of the NAO, respectively. The dynamical processes which describe the NAO are summarized with a projection analysis in section 5, followed by an analysis of the stream-function-tendency equation in section 6. The results from barotropic model calculations are presented in section 7, and the conclusions are given in section 8.

## 2. DATA AND DIAGNOSTIC TECHNIQUES

Various quantities are examined with 300 mb daily (00 UTC) data. Variables examined include the stream function, zonal and meridional wind, vorticity and divergence, and geopotential height. With the exception of geopotential height, all quantities are obtained by logarithmic interpolation of the daily National Centers for Environmental Prediction/National Center for Atmospheric Research (NCEP/NCAR) re-analysis data in sigma coordinates onto the 300 mb pressure surface. The geopotential height data

\* In this study, an anomaly is defined as the deviation of a variable from its seasonal-mean value for a particular calendar day.

† Unlike for regional anomalies such as the NAO, where the eddies are defined to be deviations from local time-mean values, for the zonal index the eddies are regarded as deviations from zonal mean values.

is obtained by integrating the hydrostatic equation upwards from the earth's surface. The NCEP/NCAR temperature field is used for this purpose. The data used cover the years from 1958 to 1997 for the months of November to March. At each grid point, the seasonal cycle is removed. The seasonal cycle is obtained by applying a 20-day low-pass digital filter to the time mean of each calendar day. All data used are at rhomboidal 30 resolution. The spatial pattern for the NAO is obtained by applying a rotated principal component analysis (RPCA) with a varimax rotation to the 300 mb geopotential height field. The covariance matrix is used. The NAO index time series is defined to be the corresponding principal component time series of the NAO.

Most studies of the NAO, and also the related annular mode or Arctic Oscillation, use mean-sea-level pressure data to define their NAO index. Although it is difficult to state which pressure level is best for defining an NAO index, in this study 300 mb height data are used for this definition simply because the results to be shown indicate that the NAO is initially driven by transient eddy vorticity fluxes in the upper troposphere. Thus an NAO index based on upper-tropospheric data appears to be more representative of the dynamical processes that drive the NAO. Nevertheless, to some extent, the choice of an index for the NAO is arbitrary, and any analysis of the life cycle of the NAO will show some sensitivity to the definition of that index.

To smooth each term in the stream-function-tendency equation slightly, a 31-point, 10-day, low-pass digital filter is applied to each term in that equation. As discussed by Feldstein (1998a, 2002) this smoothing has a negligible influence for anomalies that grow or decay within a time period as short as 5 days (as we will see, the NAO life cycle has a time-scale on the order of 2 weeks). To test the impact of this filter, some of the calculations to be presented in this study were performed with unfiltered data. For example, with unfiltered data the composite life cycle for the NAO index was found to yield a solution extremely similar to that with 10-day low-pass data, the main difference being that the results with the unfiltered data were slightly less smooth. Furthermore, this calculation showed that the time-scale of the NAO life cycle was not influenced by the filter. Thus, for the NAO, this smoothing does not alter the interpretation (Feldstein 1998a, 2002).

#### (a) *Definitions*

The method used to define persistent episodes, or NAO events, is described in detail by Feldstein (1998a, 2002). This method is based on Horel (1985) and Mo (1986). Briefly, if the pattern correlation for the geopotential height field remains above a particular threshold value for five or more consecutive days, then a persistent episode is defined to have taken place. This threshold value corresponds to the 99% confidence level for a zero null hypothesis (see Feldstein 1998a, 2002). These pattern correlations are confined to a NAO region defined as being between 30°N and the North Pole and between 90°W and 60°E. The first day of a persistent episode is defined as the onset day. The amplitude of the NAO index must exceed one standard deviation on the onset day. Also, when the NAO index is positive (negative) during a persistent episode, that particular episode is referred to as the positive (negative) phase. With these definitions, there are 43 (49) persistent episodes for the positive (negative) phase.

#### (b) *Stream-function-tendency equation*

In this study, a composite analysis of each term in the stream-function-tendency equation (Cai and van den Dool 1994; Feldstein 1998a, 2002; Franzke *et al.* 2001) is

performed. This equation can be written as

$$\frac{\partial \psi^L}{\partial t} = \sum_{i=1}^8 \xi_i + R, \quad (1)$$

where

$$\begin{aligned} \xi_1 &= \nabla^{-2} \left( -(v_r^L + v_d^L) \frac{1}{a} \frac{df}{d\theta} \right) \\ \xi_2 &= \nabla^{-2} (-[\overline{\mathbf{v}_r}] \cdot \nabla \zeta^L - \mathbf{v}_r^L \cdot \nabla [\overline{\zeta}]) + \nabla^{-2} (-[\overline{\mathbf{v}_d}] \cdot \nabla \zeta^L - \mathbf{v}_d^L \cdot \nabla [\overline{\zeta}]) \\ \xi_3 &= \nabla^{-2} (-\overline{\mathbf{v}_r}^* \cdot \nabla \zeta^L - \mathbf{v}_r^L \cdot \nabla \zeta^{*}) + \nabla^{-2} (-\overline{\mathbf{v}_d}^* \cdot \nabla \zeta^L - \mathbf{v}_d^L \cdot \nabla \zeta^{*}) \\ \xi_4 &= \nabla^{-2} \{ -(f + \overline{\zeta}) \nabla \cdot \mathbf{v}_d^L - \zeta^L \nabla \cdot \overline{\mathbf{v}_d} \} \\ \xi_5 &= \nabla^{-2} (-\mathbf{v}_r^L \cdot \nabla \zeta^L)^L + \nabla^{-2} \{ -\nabla \cdot (\mathbf{v}_d^L \zeta^L) \}^L \\ \xi_6 &= \nabla^{-2} (-\mathbf{v}_r^H \cdot \nabla \zeta^H)^L + \nabla^{-2} \{ -\nabla \cdot (\mathbf{v}_d^H \zeta^H) \}^L \\ \xi_7 &= \nabla^{-2} (-\mathbf{v}_r^L \cdot \nabla \zeta^H)^L + \nabla^{-2} \{ -\nabla \cdot (\mathbf{v}_d^L \zeta^H) \}^L + \nabla^{-2} (-\mathbf{v}_r^H \cdot \nabla \zeta^L)^L \\ &\quad + \nabla^{-2} \{ -\nabla \cdot (\mathbf{v}_d^H \zeta^L) \}^L \\ \xi_8 &= \nabla^{-2} \{ -\mathbf{k} \cdot \nabla \times (\omega^L \partial \overline{\mathbf{v}} / \partial p) \} + \nabla^{-2} \{ -\mathbf{k} \cdot \nabla \times (\overline{\omega} \partial \mathbf{v}^L / \partial p) \} \\ &\quad + \nabla^{-2} \{ -\mathbf{k} \cdot \nabla \times (\omega' \partial \mathbf{v}' / \partial p) \}^L, \end{aligned}$$

and  $\psi$  is the stream function,  $\zeta$  the relative vorticity,  $\mathbf{v}$  the horizontal wind vector,  $v$  the meridional wind component,  $\omega$  the vertical wind component,  $a$  the earth's radius,  $f$  the Coriolis parameter,  $p$  the pressure,  $\mathbf{k}$  the unit vector in the vertical direction, and  $\theta$  is latitude. The term  $R$ , which is defined as a residual, includes neglected physical processes such as frictional dissipation, and errors associated with both the interpolation from sigma onto the 300 mb pressure surface, and the use of centred time-differencing with a one day time step, rather than the individual time steps in the re-analysis model. The subscripts 'r' and 'd' denote the rotational and divergent components of the horizontal wind, respectively, and the superscripts 'H' and 'L' indicate the application of the 10-day high- and low-pass filters, respectively. The overbar denotes a time mean, a prime the deviation from the time mean, the square brackets a zonal average, and the asterisk a deviation from the zonal average. For those terms denoted with a prime, the notation indicates the sum of high- and low-frequency components. Centred time differences are used for calculation of  $\partial \psi^L / \partial t$ .

The dynamic meaning of each of the  $\xi_i$  is discussed by Feldstein (1998a, 2002). Very briefly,  $\xi_1$  corresponds to planetary vorticity advection by the anomalous meridional wind, and  $\xi_2$  and  $\xi_3$  to the relative vorticity advection that involves the interaction of the anomalies with the zonally symmetric and zonally asymmetric climatological flow, respectively. The divergence is represented by  $\xi_4$ , and the interaction amongst the low- and high-frequency transient eddies by  $\xi_5$  and  $\xi_6$ , respectively;  $\xi_7$  and  $\xi_8$  are negligible.

It is important to state that the particular decomposition of terms on the right-hand side (r.h.s.) of (1) is to a large degree arbitrary. There are many other ways of dividing the r.h.s. of (1) into various combinations of terms, and the manner in which these terms are specified will have an important impact on their interpretation. The specific aim of the decomposition used on the r.h.s. of (1) is to isolate particular nonlinear and linear processes. My motivation for investigating nonlinear processes is based on the anticipation that, like the zonal index, the NAO will also be driven by transient eddy

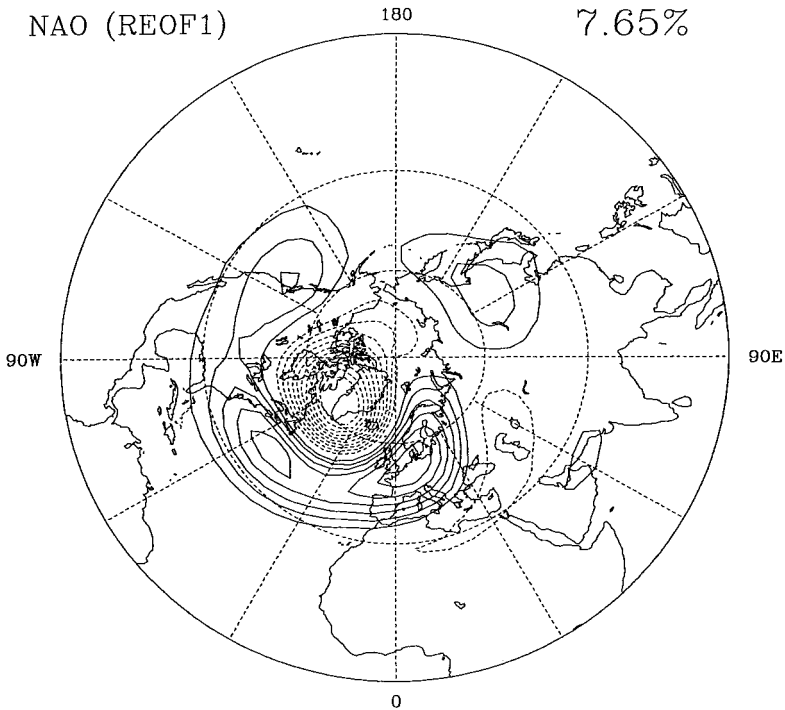


Figure 1. The unfiltered daily first rotated empirical orthogonal function (REOF1), which corresponds to the North Atlantic Oscillation (NAO). The fractional variance is shown in the upper right corner. Full contours are positive, dashed contours negative, and the zero contour is omitted. The contour interval is arbitrary.

vorticity fluxes. With regard to linear processes, one goal is to isolate the influence of the divergence term, which to some extent, as we will see, represents the secondary circulation induced by vorticity advection. In order to compare the NAO with the PNA, it is also planned to evaluate the linear interaction between the NAO anomaly and the climatological stationary eddies, since this process was found by Feldstein (2002) to be crucial during the PNA life cycle. Thus, the decomposition in (1) is chosen specifically to investigate the role of particular dynamical processes. This implies an a priori decision about which dynamical processes will receive the primary focus of attention. Nevertheless, in section 6, results with different decompositions of (1) are briefly discussed.

### 3. NAO SPATIAL STRUCTURE

The NAO spatial pattern, obtained from RPCA of the daily, unfiltered 300 mb geopotential height field, is shown in Fig. 1. The NAO corresponds to the first rotated empirical orthogonal function (REOF). A typical NAO dipole spatial pattern is seen, with one centre over southern Greenland, and another very broad centre extending across the mid-latitude North Atlantic (e.g. Barnston and Livezey 1987). For the RPCA it would have been preferable to have used stream function, rather than geopotential height. However, since an important part of this investigation will include an analysis of the stream-function-tendency equation, geopotential height is chosen for the RPCA because a similar RPCA calculation with the stream-function field did not yield the NAO

pattern amongst any of the REOFs. Perhaps this is because stream function emphasizes low-latitude variability.

As most NAO studies use either monthly or seasonal mean data, RPCA was also used to calculate the corresponding NAO pattern from monthly mean data (not shown). It was found that the daily and monthly mean NAO patterns closely resemble each other (the linear spatial correlation between the daily and monthly mean NAO patterns was 0.97). For these calculations, eight unrotated EOFs were retained. However, these results are rather insensitive to the inclusion of as many as 15 unrotated EOFs.

In order to verify that these NAO teleconnection patterns are similar to those used in other studies, the linear correlation is calculated between the monthly NAO index time series used in this study and the NAO index time series of the Climate Prediction Center (CPC) (it is the temporal and not the spatial variation of the NAO that is readily available from the CPC). For the same 200 months used in the present study, it is found that the two time series have a linear correlation of 0.80. There are several differences between the NAO index of this study and that of the CPC. For example, the NAO index from the CPC uses 700 mb monthly mean data, and their analysis is performed separately for each month, not for five continuous months as in the present study. Thus, given these many differences between the NAO index in this study and that of the CPC, this value for the linear correlation gives one confidence that one is indeed investigating the NAO teleconnection pattern.

#### 4. TEMPORAL EVOLUTION OF THE NAO

The temporal evolution of the composite anomalous 300 mb stream-function field for the NAO is shown in Fig. 2 for the positive phase and in Fig. 3 for the negative phase. For both phases the composite fields are comprised of the mean value at each lag for all persistent events (see subsection 2(a) for the definition of persistent events). Lag 0 corresponds to the onset day. Before the onset day (Figs. 2(a) to 2(c) and Figs. 3(a) to 3(c)), noticeable differences can be seen during the growth of the two phases. For example, for the positive phase, a wavetrain that extends from the central North Pacific toward the east coast of North America is present 4 days before the onset day. Although not shown, the same wavetrain is also apparent at lag  $-6$  days. This wavetrain is also robust in the sense that it is found to be present in separate composite calculations for both the first and second halves of the dataset. These results contrast with those for the negative phase where such a wavetrain is not present and the growth of the NAO anomalies appears to be primarily *in situ*. For the negative phase, although there are two anomalies in the central North Pacific at lag  $-8$  days, and two other anomalies over the USA at lag  $-4$  days, none of these four anomalies is present in separate composites from the first and second halves of the dataset.

Links between North Atlantic and North Pacific anomalies have been found in previous studies that use data that have been time-averaged beyond the bi-weekly time-scale of the NAO life cycle of the present study. For example, using monthly mean data, van Loon and Rogers (1978) and Wallace and Gutzler (1981) both show that North Pacific anomalies coincide with the NAO. However, this is not the case with all NAO studies. Furthermore, in two recent studies that use 45-day moving averaged data, Honda *et al.* (2001) and Honda and Nakamura (2001) both showed that PNA-like anomalies in the North Pacific precede the development of NAO-like anomalies. These two studies were focusing on the observed out of phase relationship between the strength of the Icelandic and Aleutian lows, which primarily occurs during the late winter.

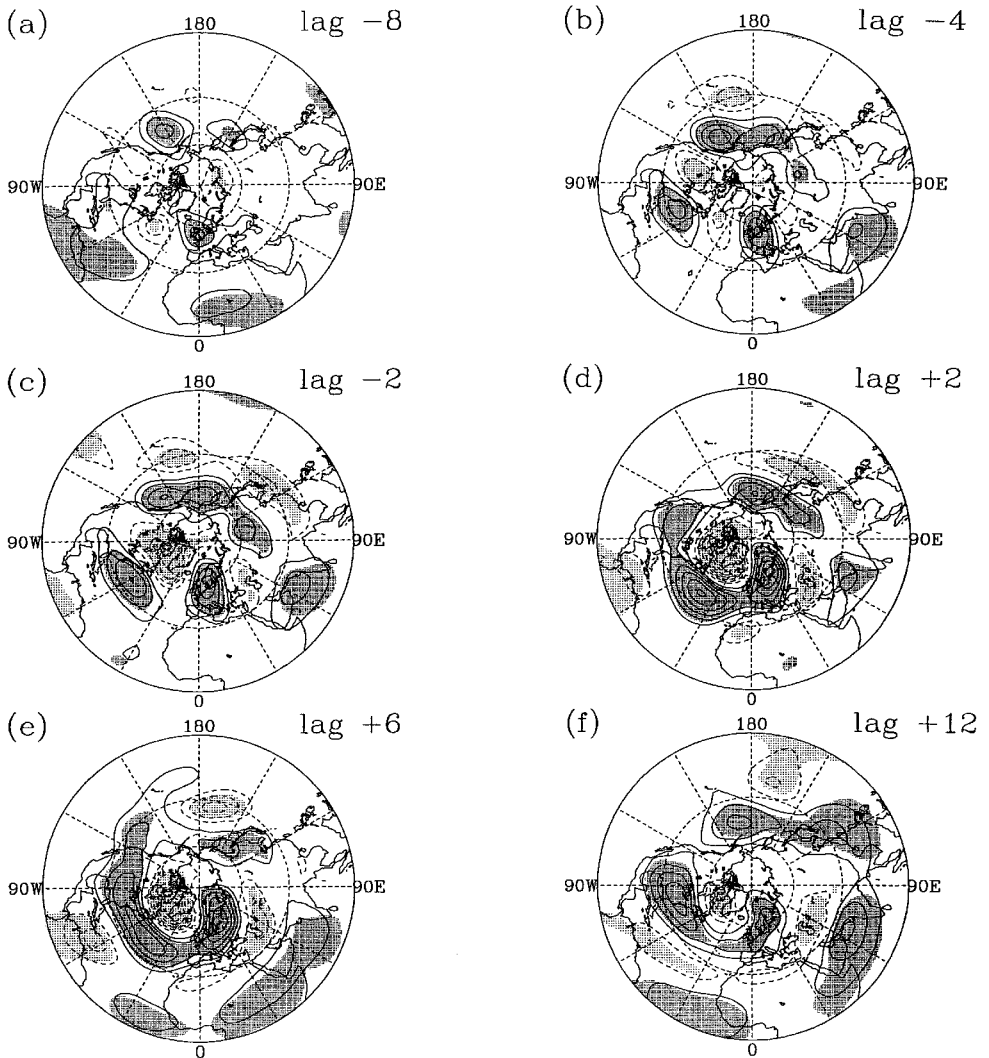


Figure 2. Composites of the positive phase anomalous 300 mb stream-function field at (a) lag  $-8$  days, (b) lag  $-4$  days, (c) lag  $-2$  days, (d) lag  $+2$  days, (e) lag  $+6$  days, and (f) lag  $+12$  days. Contour interval is  $2 \times 10^6 \text{ m}^2 \text{ s}^{-1}$ . Full contours are positive, dashed contours negative, and the zero contour is omitted. Dense (light) stippling indicates positive (negative)  $t$ -values that exceed the 95% confidence level for a two-sided  $t$ -test.

The composite calculations illustrated in Figs. 2 and 3 also reveal that the anomalies that comprise the NAO pattern arise from the propagation, merger, and amplification of anomalies that were present as far back as 8 days before onset. For example, consider the positive phase. If we examine the positive anomaly contribution towards the NAO dipole at lag  $+2$  days (Fig. 2(d)), we can trace its formation to the merger and propagation of one positive anomaly centred over western Europe and another positive anomaly centred off the east coast of the USA (Figs. 2(a) to 2(c)). Similarly, the negative anomaly contribution towards the NAO dipole is linked to the propagation and merger of one negative anomaly centred just south of Greenland and another negative anomaly located over central Canada (Fig. 2(b)). As can be seen in Fig. 3, the negative phase of the NAO is also associated with the propagation and merger of earlier existing anomalies.

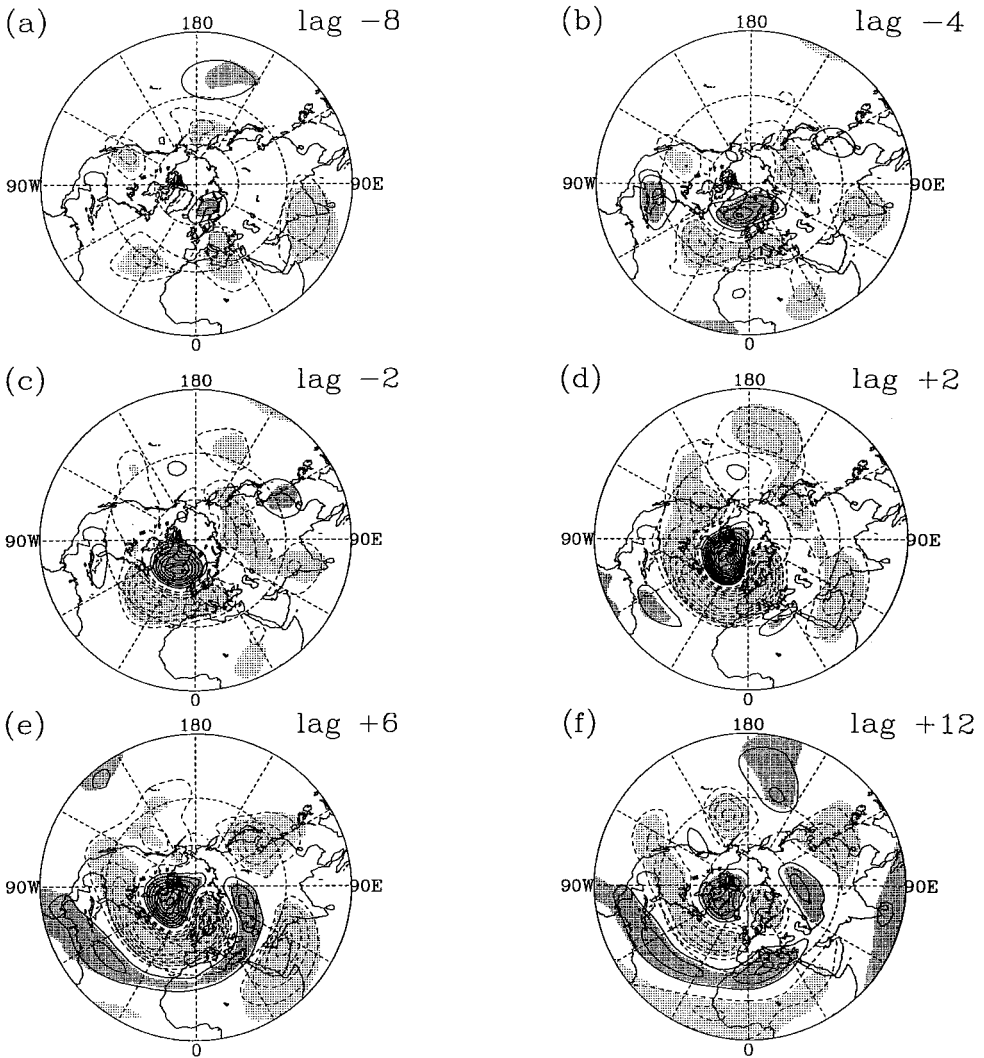


Figure 3. As for Fig. 2, except for the negative phase.

Also, the composite calculations in Figs. 2 and 3 indicate that once the anomalous NAO pattern is established, the southern anomaly becomes increasingly zonally extended over time.

Figures 2 and 3 indicate that noticeable changes occur in the spatial structure of the anomalous 300 mb stream-function field during the composite NAO life cycle, especially outside the NAO region. Thus, it is beneficial to verify that the anomalous 300 mb stream function time-averaged over the entire composite life cycle does indeed correspond closely to the REOF pattern in Fig. 1. For both phases, this time-average extends from lag -2 to lag +10 days, as this time period encompasses most of the NAO life cycle (Figs. 6(a) and 7(a)). This is shown for the positive and negative phases in Figs. 4(a) and 4(b), respectively, together with the difference between the two phases in Fig. 4(c). Each of the frames in Fig. 4 shows a stronger resemblance to the REOF pattern in Fig. 1 than does the anomalous 300 mb stream-function field at individual

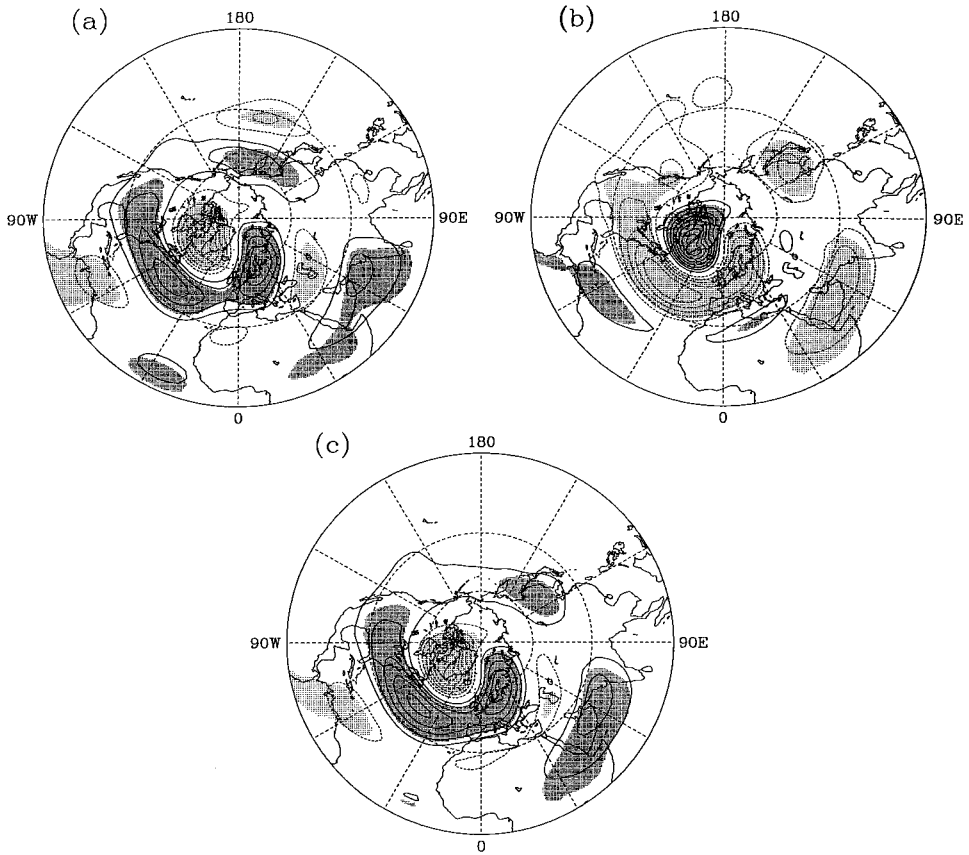


Figure 4. Time-averaged composite for (a) the positive phase, (b) the negative phase, and (c) the difference between (a) and (b). The time averaging is over the interval lag  $-2$  days to lag  $+10$  days. Contour interval is  $2 \times 10^6 \text{ m}^2 \text{ s}^{-1}$ . Full contours are positive, dashed contours negative, and the zero counter is omitted. Dense (light) stippling indicates positive (negative)  $t$ -values that exceed the 95% confidence level for a two-sided  $t$ -test.

lags in Figs. 2 and 3. As expected, the strongest similarity is between Fig. 4(c) and Fig. 1. Even the relatively weak anomalies over the Caspian and Arabian Seas and over eastern China are present in both Fig. 1 and Fig. 4(c).

The global field significance (Livezey and Chen 1983) of each of the composite patterns in Figs. 2 and 3 were also examined. To perform these calculations, a series of 1000 Monte Carlo composite patterns were first obtained. The dates for these calculations were selected at random. It was found that 5% of these patterns had more than 13.6% of their area exceed the 95% confidence level for a 2-sided  $t$ -test. For all those lags corresponding to lag  $-2$  days or later, i.e. Figs. 2(c) to 2(f) and Figs. 3(c) to 3(f), the fractional area of the anomalous stream-function field with  $t$ -values exceeding the 95% confidence level was much greater than 13.6%. For example, for the positive phase, the fractional area with  $t$ -values exceeding the 95% confidence level varies from a low value of 21% in Fig. 2(c) to a high value of 34% in Fig. 2(f). Similarly, for the negative phase, the minimum and maximum values are 21% and 44% in Figs. 3(c) and 3(f), respectively. At lag  $-4$  days, for both phases, the anomalous stream-function pattern slightly passes the field significance test, with fractional areas of 15% in Fig. 2(b) and 18% in Fig. 3(b). This suggests that the anomalous wavetrain that precedes the onset

of the positive NAO phase (Fig. 2(b)) is indeed statistically significant. On the other hand, for the negative phase, this finding suggests that the two anomalies over North America at lag  $-4$  days (Fig. 3(b)) may be statistically significant, which contrasts with the earlier result that these two anomaly centres are not present in both halves of the dataset. This contradiction likely arises from the fact that the field significance test passes by only a small amount, and because the field significance test is relevant for the overall pattern, not for individual anomaly centres, such as those over North America in Fig. 3(b). At lag  $-8$  days, for both phases, the anomalous stream-function pattern does not pass the field significance test, as the fractional areas at these lags is 10% in Fig. 2(a) and 12% in Fig. 2(b).

### 5. PROJECTIONS

The role played by each of the terms on the r.h.s. of (1) can be summarized by projecting each term on the r.h.s. of (1) onto the lag  $+3$  day composite anomalous stream-function pattern, the lag at which the composite NAO index attains its maximum value. The projection,  $P_i$ , is written as

$$P_i = \sum_j \xi_{ij}(\lambda, \theta) \psi_{Mj}(\lambda, \theta) \cos \theta, \tag{2}$$

where  $\xi_{ij}$  is the  $i$ th term on the r.h.s. of (1) and  $\psi_{Mj}$  is the composite anomalous stream-function pattern at lag  $+3$  days, both expressed at the  $j$ th gridpoint. The longitude is specified by the variable  $\lambda$ . The summation in (2) encompasses all grid points within the northern hemisphere.

To illustrate the meaning of this projection, we first write the composite anomalous stream function at any time  $t$  as

$$\psi(\lambda, \theta, t) = a(t) \psi_{Mj}(\lambda, \theta) + \psi'(\lambda, \theta, t). \tag{3}$$

By specifying  $a(t)$  to take on the form

$$a(t) = \left( \frac{\sum_j \psi(\lambda, \theta, t) \psi_{Mj}(\lambda, \theta) \cos \theta}{\sum_j \psi_{Mj}^2 \cos \theta} \right) \tag{4}$$

$\psi_{Mj}$  becomes orthogonal to  $\psi'$ , the remainder of the stream-function field. Next, we substitute (3) into (1), multiply both sides of (1) by  $\psi_{Mj} \cos(\theta)$ , and integrate over the entire northern hemisphere. Neglecting the residual,  $R$ , in (1) and using the above orthogonality property yields

$$\frac{da}{dt} = \frac{\sum_{i=1}^8 P_i}{\sum_j \psi_{Mj}^2 \cos \theta}. \tag{5}$$

This result allows us to interpret the projection in (2) as representing the influence of individual  $\xi_i$  on the rate of change with time of  $a(t)$ . Also, although the above derivation involves an integration over the entire northern hemisphere, the same methodology applies to any particular domain. When the projection results to be presented below were compared with those limited to the NAO region, the differences were found to be slight, i.e. the projection values for the entire northern hemisphere differed from those limited to the NAO region by less than 20%, for most quantities at most lags.

By comparing the full projection in (5), i.e. the r.h.s. of (1) with the residual neglected, to the projection of  $\partial\psi/\partial t$  onto  $\psi_{Mj}$ , we can determine the size of the

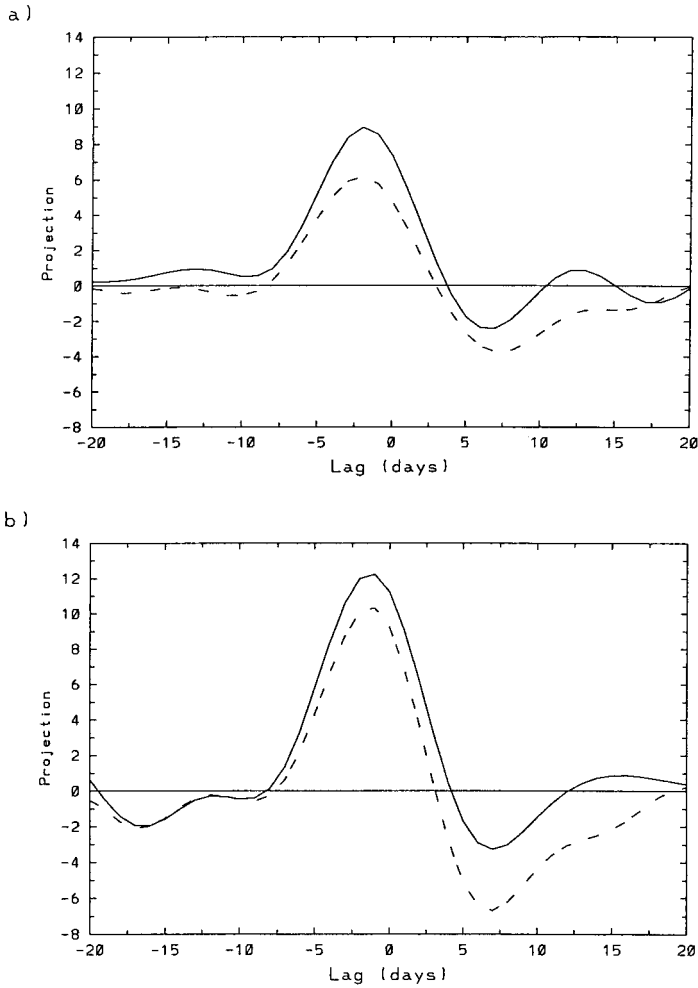


Figure 5. Projections of  $\partial\psi/\partial t$  (dashed line) and the right-hand side of (1) with the residual neglected (full line) onto  $\psi_{Mj}$  (see text) for (a) the positive phase and (b) the negative phase of the North Atlantic Oscillation. The values in the ordinate have been multiplied by  $5 \times 10^6 \text{ s}^{-1}$ .

residual, or the error, in the projection. This is illustrated in Fig. 5 for both NAO phases. As can be seen, although the balance is very good at many lags, at some lags there are indeed fairly large errors present. This is most apparent near the time of the maximum growth of the positive phase, and towards the end of the decay of the negative phase. As discussed in subsection 2(b), likely sources for this error include the interpolation from sigma to pressure coordinates and the use of daily data for the time-differencing rather than data at every re-analysis model time step. This indicates that the error can involve either one or both sides of (1).

Before examining the projections, the composite evolutions are shown in Figs. 6(a) and 7(a) of  $a(t)$  for the positive and negative phases, respectively. As can be seen, for both phases,  $a(t)$  completes its life cycle of growth and decay within a time period of

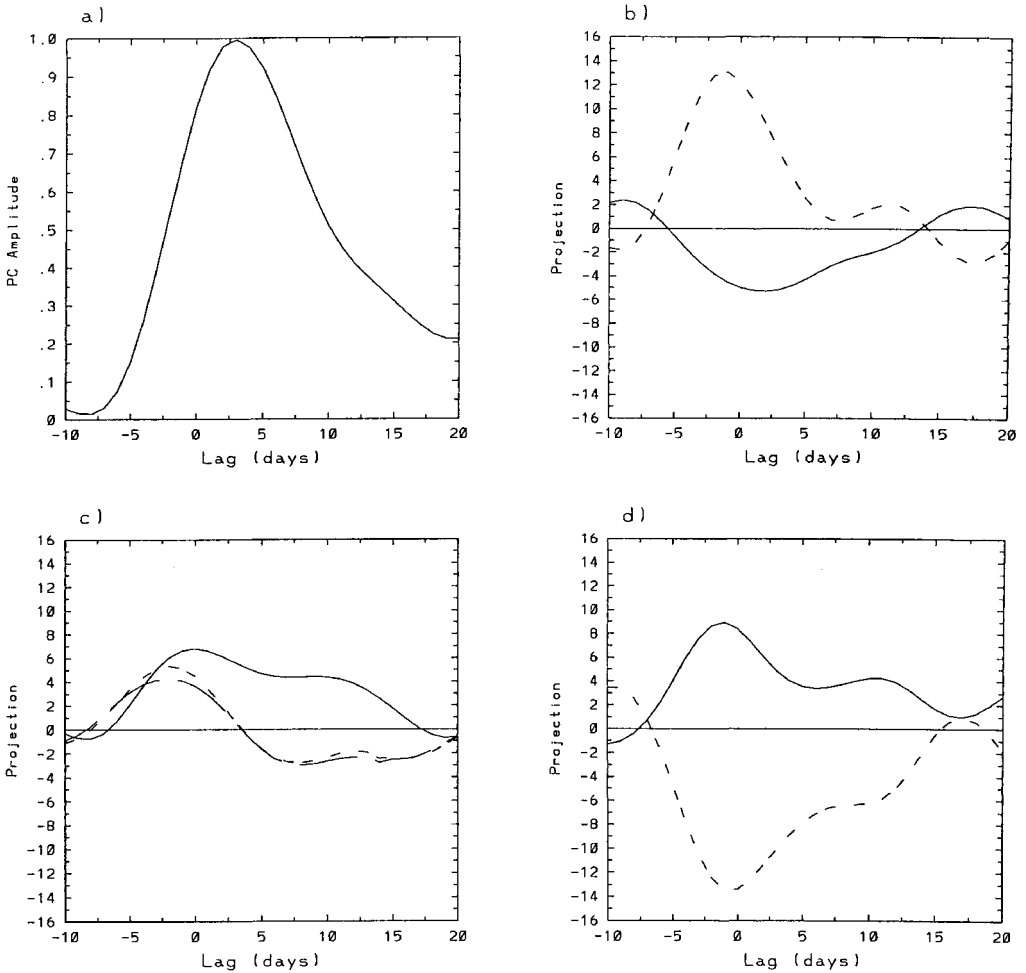


Figure 6. (a) Composite time series of  $a(t)$  (see text) for the positive phase of the North Atlantic Oscillation. Time lagged projections of the following combinations of terms onto  $\psi_{Mj}$ : (b) full line  $\sum_{i=5}^6 \xi_i$ ; (c) full line  $\xi_6$ , short dashed line  $\xi_5$ , long dashed line,  $\xi_5$  with the self-interaction subtracted; and (d) full line  $\sum_{i=1}^3 \xi_i$ , dashed line  $\xi_4$ . In (a), the ordinate is nondimensional, and in (b), (c), and (d) the ordinate has been multiplied by  $5 \times 10^6 \text{ s}^{-1}$ . See text for explanation of symbols.

about 2 weeks\*. Such a time-scale is very similar to that for the life cycle of the zonal index, as discussed in the introduction.

The projections for both phases of the entire NAO life cycle are found to be rather similar (see Figs. 6 and 7). The key features are summarized in Figs. 6(b) and 7(b), which show that the growth of the NAO is driven by nonlinear processes, i.e.  $\xi_5 + \xi_6$ , and the decay of the NAO arises primarily from linear processes,  $\sum_{i=1}^4 \xi_i$ . A decomposition of the nonlinear terms (Figs. 6(c) and 7(c)) indicates that both the high- and low-frequency transient eddy vorticity fluxes drive the NAO during the growth stage. Furthermore, Figs. 6(c) and 7(c), together with Figs. 6(d) and 7(d), reveal that the NAO decay is

\* Although not shown, the composite temporal evolution of the NAO index is almost identical to that of  $a(t)$ , as the linear correlation between the composite NAO index time series and the composite  $a(t)$  is greater than 0.99 for both phases.

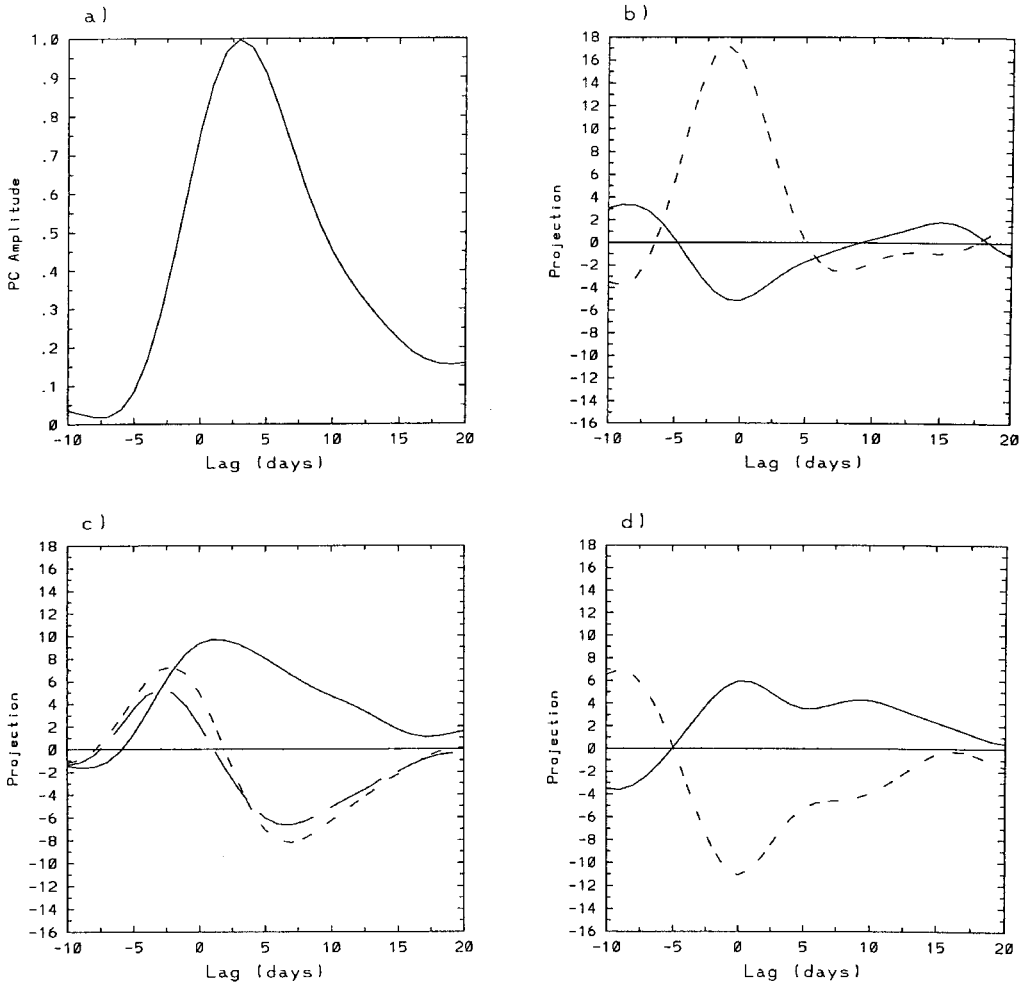


Figure 7. As for Fig. 6, except for the negative phase.

primarily due to the divergence term, with the low-frequency transient eddy vorticity fluxes also contributing. In addition, throughout the NAO decay, the high-frequency transient eddy vorticity fluxes act to maintain the NAO anomaly. Such behaviour is consistent with the high-frequency transient eddies being involved in a positive feedback after the NAO anomaly is established. Inspection of the projections associated with the nonlinear processes, i.e.  $\xi_5 + \xi_6$ , with that of the divergence term,  $\xi_4$ , indicates a tendency for these projections to cancel one another at most lags before lag +6 days, i.e. during that time period when the NAO anomaly is growing and the early stages of the NAO anomaly decay. As can be seen in Figs. 6 and 7, this cancellation is stronger for the positive phase. Also, a comparison of the spatial structure of  $\xi_4$  with that of  $\xi_5 + \xi_6$  (not shown) indicates a stronger tendency for these terms to cancel each other within the NAO region than outside the region. A physical interpretation of this cancellation is presented in section 7.

Also examined is the contribution of the composite stream-function anomaly towards the projection by the low-frequency transient eddy vorticity fluxes. This is

illustrated in Figs. 6(c) and 7(c), which show the projection of the ‘self-interaction’, i.e.  $\nabla^{-2}(-\mathbf{v}_{rC}^L \cdot \nabla \zeta_C^L)$  subtracted from  $\xi_5$ . In this equation, the subscript C denotes composite stream-function anomaly. As can be seen, the self-interaction of the NAO plays little role towards the growth and the decay of the NAO.

(a) *Relationship between the NAO and the zonal index*

As discussed in the introduction, there is a high correlation between the ZI and the NAO index time series. This result leads one to anticipate that there would be large similarities between the dynamical processes that account for the growth and decay of the ZI and that of the NAO. Since the ZI is a zonal mean quantity, instead of using (1) which is applicable for regional phenomena such as the NAO, consider the composite zonal-mean-momentum equation with only the eddy momentum flux convergence term retained, i.e.

$$\frac{\partial [u]_C}{\partial t} = -\frac{\partial [\overline{u^* v_C^*}]}{\partial y} - \frac{\partial [u_C^* \overline{v^*}]}{\partial y} - \frac{\partial [u'^* v'^*]_C}{\partial y}. \quad (6)$$

The tendency equation for the ZI can easily be obtained by projecting each term in (6) onto the EOF spatial pattern of the ZI. The notation in (6) is the same as that used to describe (1). As in the above paragraph, the subscript C denotes a composite anomaly. The first two terms on the r.h.s. of (6) correspond to the interaction between the composite  $u^*$  and  $v^*$  winds with those of the climatological stationary eddies, and the third term on the r.h.s. of (6) involves the interaction amongst all  $u^*$  and  $v^*$  transient eddies. It is important to keep in mind that each of the eddy variables on the r.h.s. of (6) are deviations from the zonal mean flow. Also, the variables  $u^*$  and  $v^*$  in the third term on the r.h.s. of (6) represent all anomalies including the composite. Equation (6) contrasts with (1), for which the eddies are deviations from the local time mean flow. Thus, none of the three terms on the r.h.s. of (6) correspond to particular terms on the r.h.s. of (1).

The question of how to interpret the high linear correlation between the ZI and NAO time series is now addressed, given that the NAO and ZI are mathematically described by different equations. As stated in the introduction, DeWeaver and Nigam (2000a, 2000b) and Feldstein and Lee (1998) showed that the first two terms on the r.h.s. of (6) contribute substantially towards the growth and maintenance of the ZI anomaly. Since  $u_C^{/*}$  and  $v_C^{/*}$  in (6) are simply the  $u$  and  $v$  components of the NAO anomaly with the zonal mean subtracted, and because our projection calculations suggest that the NAO anomaly is driven by local transient eddies, i.e. transient eddies that are confined to the North Atlantic and surrounding regions (see Figs. 8(c), 8(d), and 8(e)), it is inferred that the ZI must ultimately be driven by the local transient eddies.

To examine the role of this interaction between the NAO anomaly and the climatological stationary eddies, both the left-hand side (l.h.s) of (6) and the sum of the first two terms on the r.h.s. of (6) are projected onto the composite zonal mean zonal wind anomaly at lag +3 days (the lag at which the NAO index attains its largest amplitude). The results were found to be similar to those of Feldstein (1998b), who found that this interaction between the climatological stationary and transient eddies, i.e. the first two terms on the r.h.s. of (6), accounted for about 50% of the growth of the zonal mean zonal wind anomaly. Thus, the high correlation between the ZI and the NAO can be understood as arising from the ZI being driven in large part by the interaction of the NAO with the climatological stationary eddies. Furthermore, as suggested by Fig. 7 of Feldstein (1998b), it is this interaction that contributes to the maintenance of the ZI against the affects of dissipation.

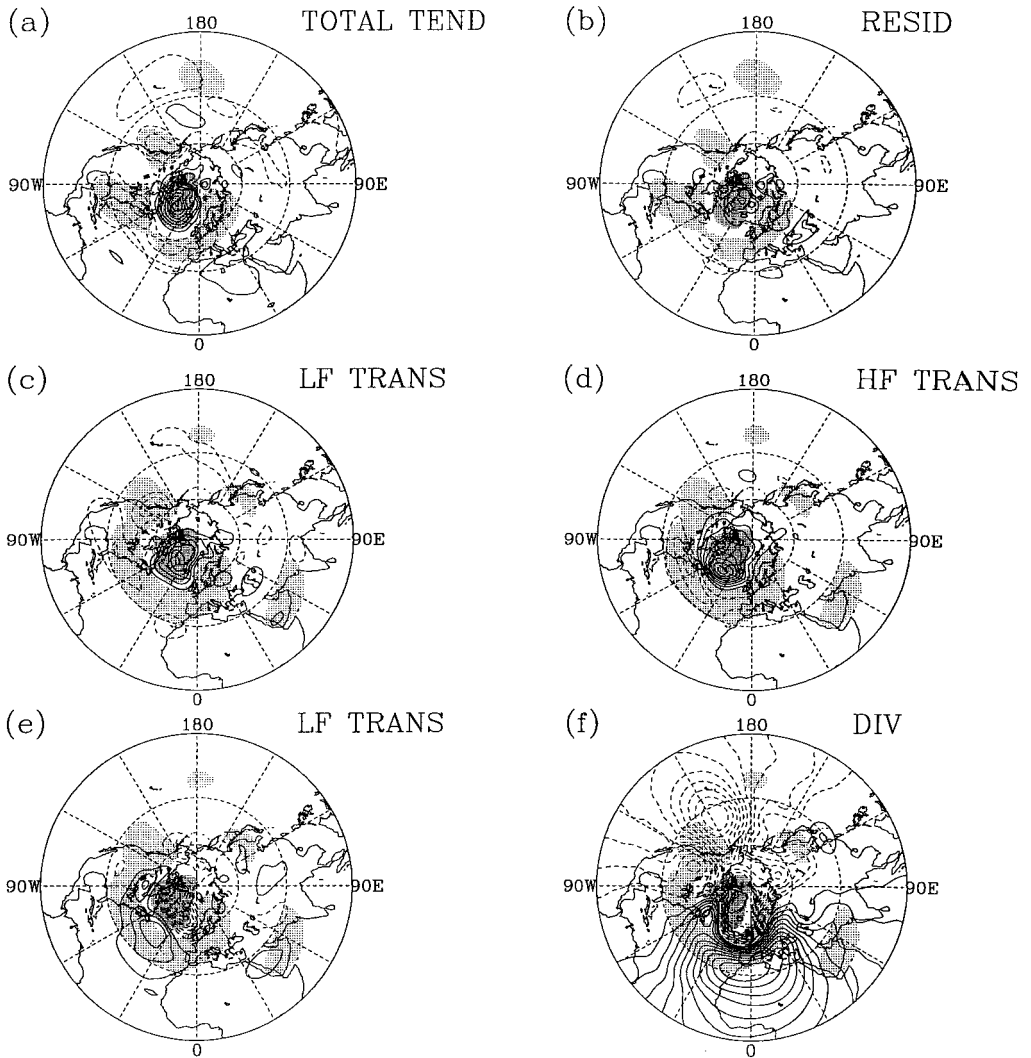


Figure 8. Composites of various combinations of terms on the right-hand side of (1): (a) the sum of all terms of the right-hand side of (1), i.e.  $\sum_{i=1}^8 \xi_i$ , at lag  $-2$  days, (b) the residual  $R$  at lag  $-2$  days, (c)  $\xi_5$  at lag  $-2$  days, (d)  $\xi_6$  at lag  $+2$  days, (e)  $\xi_5$  at lag  $+6$  days, and (f)  $\xi_4$  at lag  $0$ . (See text for explanation of symbols.) The contour interval is  $10.0 \text{ m}^2 \text{ s}^{-2}$ . Full contours are positive, dashed contours negative, and the zero contour is omitted. Dense (light) stippling indicates positive (negative) values of the anomalous 300 mb stream-function tendency in (a) and (b) and the anomalous 300 mb stream function at lag  $+3$  days in (c) to (f). The stippling is above a magnitude of  $10.0 \text{ m}^2 \text{ s}^{-2}$  in (a) and (b) and above  $4.0 \times 10^6 \text{ m}^2 \text{ s}^{-1}$  in (c) to (f).

### (b) Comparison with the PNA

The projections in Figs. 6 and 7 also indicate important differences between the growth stage of the NAO and that of the PNA. For example, Feldstein (2002) found that the linear terms in (1), i.e.  $\sum_{i=1}^4 \xi_i$ , dominate the growth of the PNA. This contrasts with our earlier results which showed that the NAO growth is driven by nonlinear processes, i.e.  $\xi_5 + \xi_6$ . In particular, the growth of the PNA was primarily due to  $\xi_3$ , which represents the interaction of the low-frequency anomaly with the zonally asymmetric component of the climatological flow. For the NAO, the projections associated with  $\xi_3$

were found to be relatively minor (although not shown, the  $\xi_3$  projection was found to contribute to the NAO growth with a maximum amplitude of about one-fifth that of the sum of the nonlinear terms). There are also some similarities between the NAO and the PNA. For example, as shown in Figs. 6(d) and 7(d), and by Feldstein (2002), the decay of both the NAO and PNA are dominated by the influence of the divergence term. Another important similarity between the NAO and PNA is that the high-frequency transient eddies appear to be maintaining the anomalies via a positive feedback process (see Feldstein 2002).

### (c) *Limitations*

As discussed by Feldstein (2002), one limitation of the projection technique is that it involves a specific spatial pattern, i.e.  $\psi_{Mj}$ , rather than the composite stream-function field whose spatial pattern changes with time. The advantages of this technique, over that of projecting onto the instantaneous anomaly pattern, is that it is amenable to straightforward interpretation through (5). To assess this limitation, projections onto the instantaneous anomalous 300 mb stream-function field were also performed. Although not shown, the results are qualitatively very similar to those shown in Figs. 6 and 7. However, there is one important exception. This is that the instantaneous projections by both the high- and low-frequency transient eddy vorticity fluxes remain positive as early as lag  $-10$  days. This result suggests that the anomaly field that precedes the onset of the NAO, which as shown in Figs. 2 and 3, has a spatial pattern that is different from that of the NAO, is also driven by transient eddy vorticity fluxes in both frequency bands.

## 6. STREAM-FUNCTION-TENDENCY EQUATION

The spatial structure of the key terms on the r.h.s of (1) is now examined. Although the projection plots of Figs. 6 and 7 yield the essential information, it is beneficial to examine the spatial structure of these terms in order to verify that the projections are indeed associated with the NAO and are not simply a small residual arising from contributions throughout the hemisphere. Since the results for both phases are qualitatively similar by the time that the NAO anomaly is established, i.e. by lag  $-2$  days, only the results for the negative phase are shown. We begin by examining the degree to which the budget is balanced (Figs. 8(a) and 8(b)). In Fig. 8(a), the sum of the terms on the r.h.s of (1) (illustrated with contours) with the residual neglected is compared with the stream-function tendency (shown with shading). The corresponding difference between these quantities, i.e. the residual, is shown in Fig. 8(b). For Figs. 8(a) and 8(b), lag  $-2$  days is selected, since that is the lag with the largest anomaly growth (Fig. 7(b)). Overall, it can be seen that the residual is relatively small in the NAO region and, elsewhere, its largest value reaches about one-third that of the maximum stream-function tendency. A residual of this magnitude had already been alluded to from the projection calculations in Fig. 5.

As the dominant terms in the projections are those by the high- and low-frequency transient eddy vorticity fluxes, and the divergence term, these quantities are illustrated at those lags where their projections attain extreme values. For the low-frequency transient eddy vorticity fluxes, as can be seen in Figs. 8(c) and 8(e), this quantity does project positively onto  $\psi_{Mj}$  at lag  $-2$  days and negatively onto  $\psi_{Mj}$  at lag  $+6$  days, respectively. Similarly, at lag  $+2$  days, the high-frequency transient eddy vorticity fluxes project positively onto  $\psi_{Mj}$  and at lag 0 the divergence term projects negatively onto  $\psi_{Mj}$ , again consistent with the projections in Figs. 7(c) and 7(d), respectively. In a manner similar to that for the PNA (Feldstein 2002), the structure of the low-frequency transient

eddy fluxes undergoes substantial change throughout the life cycle, whereas the high-frequency transient fluxes undergo little change. In addition, before the establishment of the positive phase of the NAO, as shown in Fig. 2(b), an upstream wavetrain is present. An examination of the various terms on the r.h.s. of (1) indicates that this wavetrain is also driven by the high-frequency transient eddy vorticity fluxes. With regard to the divergence term, throughout the NAO life cycle, the changes in the spatial structure of this term are rather small, the most prominent being changes in the relative amplitude of the positive and negative contributions (not shown).

As discussed in section 2, the decomposition of terms specified on the r.h.s. of (1) is arbitrary. The results are briefly analysed with three other selected decompositions of the r.h.s. of (1). For the first example, the role of the Rossby wave source (Sardeshmukh and Hoskins 1988) is examined, which is described by the advection of the climatological absolute-vorticity field by the anomalous divergent wind field. Such a calculation involves terms that are included within  $\xi_1$ ,  $\xi_2$ , and  $\xi_3$ , and thus cannot be identified with the decomposition on the r.h.s. of (1). Analysis of the Rossby wave source finds that this process attains its largest influence when the NAO anomaly begins its decay. Furthermore, this process has a relatively small maximum amplitude being of about one-half that of  $\xi_1$  and  $\xi_2$ . For the second example, the influence of shearing and stretching of the anomaly by the climatological flow are calculated. The terms that correspond to this process are represented by the advection of anomalous vorticity by the climatological wind field, which are included within both  $\xi_2$  and  $\xi_3$ . The calculation finds that the influence of shearing and stretching is as substantial as that of  $\xi_1$  and  $\xi_2$ . A detailed analysis of a particular process is beyond the scope of this study. Lastly, as will be seen, there is a tendency for the sum of the terms  $\xi_4$ ,  $\xi_5$ , and  $\xi_6$  to be small, especially when the NAO anomaly is growing. In this study, these three terms are computed separately. If they were combined, one could be left with the impression that linear and nonlinear processes play a similar role during the NAO growth. However, since the anomalous divergence is to some degree induced by the anomalous transient eddy vorticity fluxes, as described in the next section, and because the anomalous divergence would be different if the eddy fluxes were absent, one could also argue whether or not the divergence should be separately examined.

## 7. BAROTROPIC MODEL RESULTS

Next the NAO evolution is examined with the forced, nonlinear, barotropic vorticity equation on the sphere. As used by Feldstein (2002), this model is used in order to isolate the role of individual terms on the r.h.s. of (1) during various stages of the NAO evolution. The methodology used is identical to that by Feldstein (2002), and so the model will only be briefly described. The barotropic vorticity equation can be written as

$$\frac{\partial \nabla^2 \psi'}{\partial t} + \{J(\psi', \nabla^2 \bar{\psi} + f) + J(\bar{\psi}, \nabla^2 \psi') + J(\psi', \nabla^2 \psi')\} = -\nu \nabla^{10} \psi' + F, \quad (7)$$

where  $\psi'$  is the instantaneous stream-function anomaly,  $\bar{\psi}$  the November through March climatological stream function,  $f$  the Coriolis parameter,  $J$  the Jacobian operator,  $\nu$  the horizontal diffusion coefficient, and  $F$  is external forcing. As discussed by Feldstein (2002), the first three linear terms in (1), i.e.  $\sum_{i=1}^3 \xi_i$ , correspond to the linear Jacobian terms in (7), and the self-interaction contribution to  $\xi_5$  corresponds to the nonlinear Jacobian term in (7). The forcing term  $F$ , on the r.h.s. of (7), represents the summation of three terms on the r.h.s. of (1),  $\sum_{i=4}^6 \xi_i$ , i.e. the high-frequency driving, the low-frequency interaction with the self-interaction subtracted, and the divergence term.

For this model, rhomboidal 30 resolution is used, and  $\nu = 8 \times 10^{37} \text{ m}^8 \text{ s}^{-1}$ . Only the results for the negative phase are described, as the qualitative differences for the two phases are relatively small for the life-cycle stages to be described below. The initial stream-function anomaly corresponds to the composite anomalous stream function at a particular lag, and the model is integrated for 4 days. The model solution is then compared with the composite field that corresponds to the end of the model integration. Because of the presence of the nonlinear Jacobian in (7), the model solution is expected to differ from the composite by some amount. This simply reflects the property that although the life cycle for any individual event would be expected to be a solution of (7), one could not expect the composite of these life cycles also to be a solution of (7). Another source of potential error involves the property that for the forcing term,  $F$ , composite values are used. Because the composite forcing terms are available only with daily data, linear interpolation for intermediate time steps must be used (there are 48 model time steps per day). As we will see, the influence of the nonlinear Jacobian in (7) is small, and the model solution does indeed compare favourably with the composite field, implying that these two errors sources are relatively small.

### (a) *Growth stage*

We first examine the results from barotropic model integrations for the growth stage, which is defined as the time period extending from lag  $-4$  days until onset. For this calculation the initial flow corresponds to that illustrated in Fig. 3(b). Six separate model integrations are performed. In two of these integrations  $F$  is set equal to zero, and the nonlinear Jacobian term is either included or excluded. Three of the model integrations are characterized by retaining just one of the forcing terms described at the beginning of this section, and the remaining model integration includes all three forcing terms and the residual (for this calculation the residual is defined to include  $\xi_7$  and  $\xi_8$ ). The results are illustrated in Fig. 9. When all the forcing terms and the residual are included (Fig. 9(f)), the model integration yields a pattern reasonably similar to the observed composite stream-function-anomaly field on the onset day (Fig. 11(a)). The spatial correlation between the anomaly patterns in Fig. 9(f) and Fig. 11(a) is 0.83 for the NAO region.

The unforced solutions (Figs. 9(a) and 9(b)) indicate that the self-interaction by the anomaly field has little influence on the linear integration. Furthermore, if Figs. 9(a) and 9(b) are compared with Fig. 3(b), the anomalous stream-function field for the start of the model integration, it can be seen that in the NAO region the primary linear influence is the downstream advection of the anomaly field. An examination of the role of the high- and low-frequency vorticity fluxes (Figs. 9(c) and 9(e)) shows that both of these terms amplify the anomaly, with the former term appearing to cause the NAO anomaly to become increasingly zonally extended over time, as described in section 4. Furthermore, the divergence term dampens the anomaly, as indicated by the complete sign reversal of the anomaly (Fig. 9(d)).

As discussed by Feldstein (2002), the anomalous divergence term shows characteristics that allow us to interpret this term in part as corresponding to the secondary circulation that arises as a response to vorticity advection, in order to maintain thermal-wind balance (Holton 1992). For example, comparison of Figs. 9(a) and 9(d) shows that the anomalous divergence contributes to upstream propagation of most anomaly centres. This suggests that the linear vorticity advection induces a secondary circulation which opposes its tendency to advect anomalies downstream. In a similar manner, the high- and low-frequency transient eddy vorticity fluxes will also drive a secondary circulation that opposes the influence of these fluxes. Results consistent with this viewpoint can be

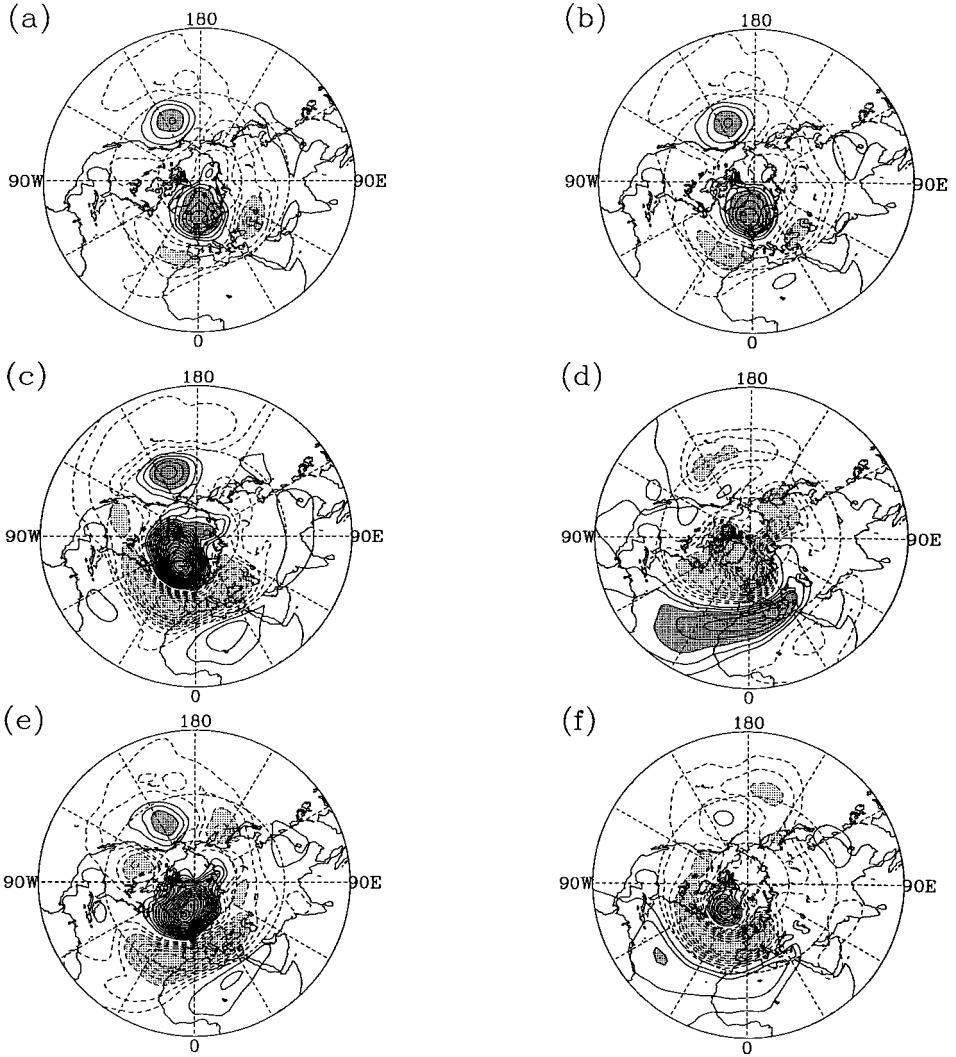


Figure 9. Anomalous stream-function field for the four-day barotropic model integration. Start date is lag  $-4$  days. The results shown are for (a) the unforced linear model,  $J(\psi', \nabla^2 \psi') = 0$  and  $F = 0$ , (b) the unforced nonlinear model,  $J(\psi', \nabla^2 \psi') \neq 0$  and  $F = 0$ , (c) the forced nonlinear model only with  $\xi_6 \neq 0$ , (d) the forced nonlinear model only with  $\xi_4 \neq 0$ , (e) the forced nonlinear model with  $\xi_5 \neq 0$  and the self-interaction subtracted, and (f) the forced nonlinear model with  $\xi_4, \xi_5$ , and  $\xi_6$  all nonzero. The residual term,  $R$ , from (1) is also included amongst the forcing terms in (f). The contour interval is  $2 \times 10^6 \text{ m}^2 \text{ s}^{-1}$ . Full contours are positive, dashed contours negative, and the zero contour is omitted. Dense (light) stippling denotes positive (negative) values with a magnitude in excess of  $6 \times 10^6 \text{ m}^2 \text{ s}^{-1}$ . (See text for explanation of symbols.)

seen by comparing Figs. 9(c) and 9(e) with Fig. 9(d), where it is shown that the influence of the driving by both sets of eddy fluxes is opposed by that of the divergence term. This tendency for the sum of the influence of the high- and low-frequency transient eddies to be opposed by that due to the divergence term, or equivalently the secondary circulation, was also indicated in the projections by these quantities in Figs. 6 and 7, as discussed in section 5.

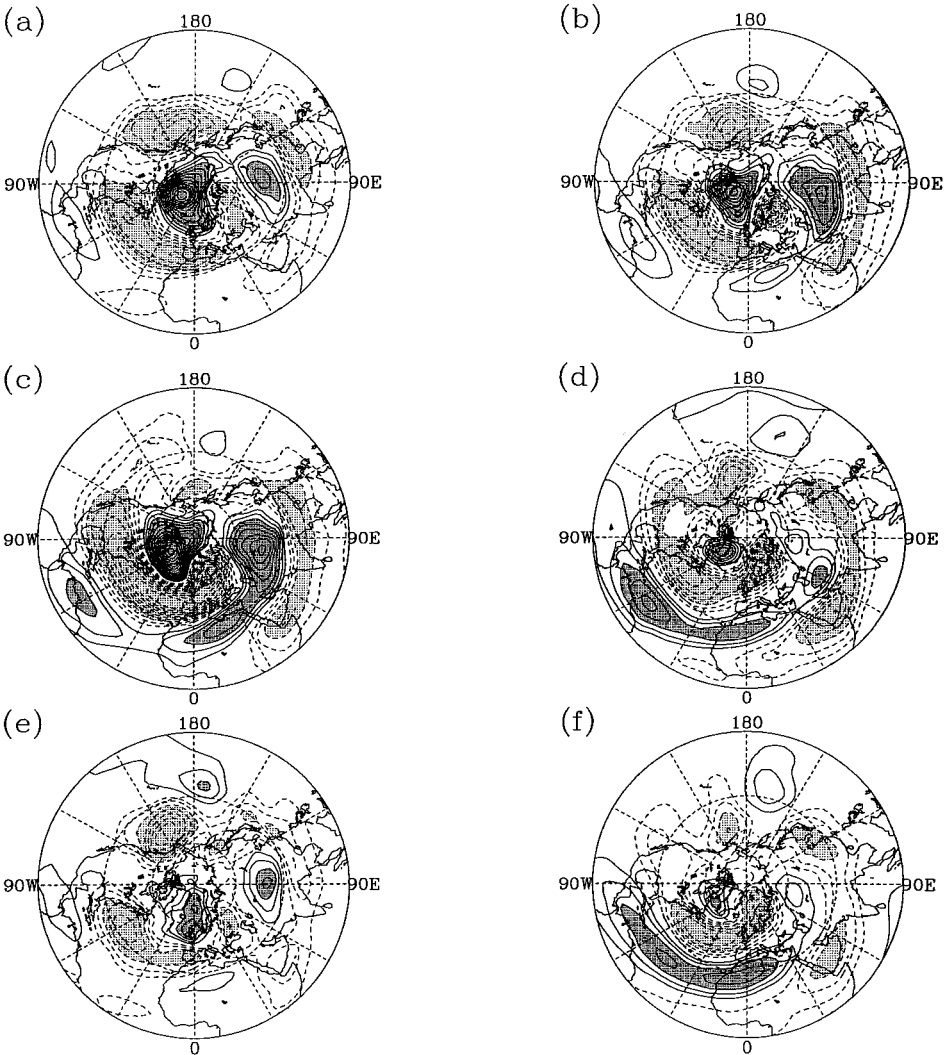


Figure 10. As for Fig. 9, except with a start date of lag +6 days.

(b) *Decay stage*

We next examine the results from the barotropic model for the decay stage, defined as being between lag +6 and lag +10 days (Fig. 10). For this calculation, the initial flow is shown in Fig. 3(e). Once again, the barotropic model results (Fig. 10(f)) compare well with the observed composite field (Fig. 11(b)), with the spatial correlation between these two fields within the NAO region being 0.90.

During the decay stage, as seen in Figs. 10(a) and 10(b), the unforced solutions do not account for much of the anomaly decay. Furthermore, as expected from the projections (Fig. 6), the high-frequency transient eddy fluxes continue to amplify the NAO anomaly, whereas the low-frequency transient eddy fluxes and the divergence term contribute towards the anomaly decay. This can be seen by comparing the spatial patterns in Figs. 10(c), 10(d), and 10(e) with that at the beginning of the model

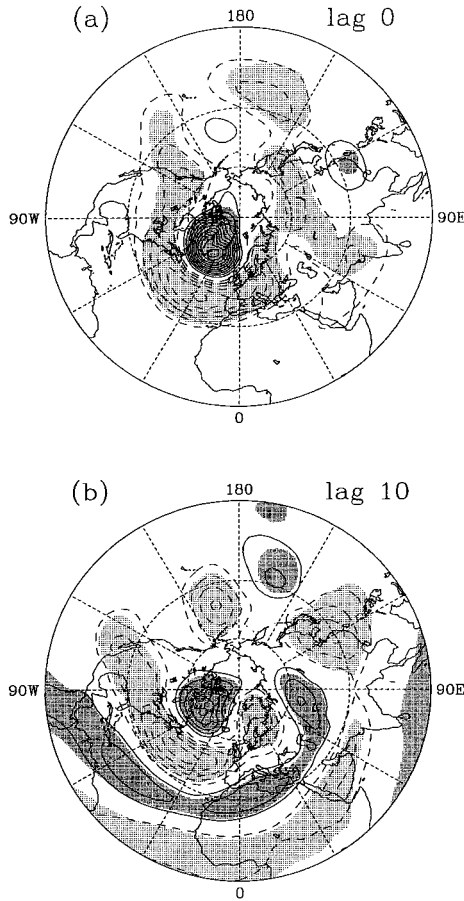


Figure 11. Composites of the negative phase of the North Atlantic Oscillation anomalous 300 mb stream-function field at (a) lag 0, and (b) lag +10 days. Contour interval is  $2 \times 10^6 \text{ m}^2 \text{ s}^{-1}$ . Full contours are positive, dashed contours negative, and the zero contour is omitted. Dense (light) stippling indicates positive (negative)  $t$ -values that exceed the 95% confidence level for a two-sided  $t$ -test.

integration (Fig. 3(e)). Figure 10(c) shows a spatial pattern with a larger amplitude than that in Fig. 3(e), whereas the amplitude of the patterns in Figs. 10(d) and 10(e) are smaller than that in Fig. 3(e). From these results, it is inferred that part of the driving of the secondary circulation is by the high-frequency transient eddy fluxes. Also, since the low-frequency eddies are contributing to the decay of the NAO anomaly, it is likely that the influence of these particular eddy fluxes on the secondary circulation opposes that of the high-frequency eddies. In addition, equatorward of the NAO region, these results suggest that the stream-function anomalies in that region arise primarily from the response by the secondary circulation to the driving by the high-frequency transient eddy fluxes, with linear dispersion playing a relatively minor role.

These model results, together with other properties of the observed flow, suggest that Ekman pumping may be the cause of the NAO decay. For example, one requirement for Ekman pumping being the cause of the NAO decay is for the spatial pattern of the anomalous surface pressure field to resemble closely that of the anomalous 300 mb stream-function field. This is because Ekman pumping must be associated with a deep vertical circulation that extends down to the surface. For the anomalous surface pressure

field, this property is indeed found to be the case at all lags during the NAO life cycle (not shown). In fact, the amplitude of the NAO surface pressure anomaly is about four times greater than that for the PNA (Feldstein 2002). It is likely that to some extent this difference is due to the NAO having a larger Rossby penetration depth because of its greater horizontal scale. Thus, although these results do not rule out other processes, such as thermal advection, eddy heat fluxes, and diabatic heating as contributing toward the NAO decay, these results do strongly hint that Ekman pumping is indeed important for the decay of the NAO. Additional support for the role of Ekman pumping also comes from other ZI studies, e.g. Robinson (1996, 2000), where it is shown that surface friction plays a crucial role in the ZI life cycle.

## 8. CONCLUSIONS

In this study, the dynamical processes that drive the NAO are investigated. With the use of composites, projections, and barotropic model calculations, all associated with the stream-function-tendency equation, a rather simple picture for the NAO life cycle is presented. This is that the NAO growth is driven by both high- and low-frequency transient eddy vorticity fluxes, and that the decay of the NAO is due to both the influence of the low-frequency eddy fluxes and Ekman pumping. The entire life cycle is complete within approximately two weeks. However, it is crucial to emphasize that this claim for Ekman pumping is qualitative and is certainly not definitive. Furthermore, the results suggest that the NAO life cycle is prolonged by a positive feedback processes involving the NAO anomaly and the high-frequency transient eddy vorticity fluxes. Although the above results apply to both phases of the NAO, it is found that for the positive NAO phase the anomaly is initiated by a remote wavetrain from the North Pacific. This contrasts with the negative NAO which shows *in situ* growth.

The relationship between the NAO and ZI was also investigated. It was found that the NAO pattern interacts with the climatological stationary eddy field to excite the ZI. It is this interaction that relates the NAO to the ZI.

The results of this study might also have implications for the relationship between the NAO and the so-called annular mode (Thompson and Wallace 1998, 2000), the first EOF of the sea-level-pressure field. The annular mode takes on a dipole spatial structure with one sign over the polar cap and opposite polarity in middle latitudes. Thus, the annular mode has a strong zonally symmetric component. Within the North Atlantic, the annular mode and NAO take on a very similar spatial structure. The amplitude of the annular mode is also highly correlated with the NAO index; e.g. Ambaum *et al.* (2001) find a temporal correlation of 0.92. Over the past few years a debate has arisen as to whether the NAO or the annular mode is a more appropriate paradigm of low-frequency variability (Wallace 2000; Deser 2000; Ambaum *et al.* 2001). As shown in Figs. 2 and 3, the NAO is initially confined to the North Atlantic, but during its decay the anomaly pattern becomes increasingly zonally extended as it expands westward into the North Pacific Ocean. This suggests that perhaps the northern hemisphere annular mode may simply be representing the decay stage of the NAO. Such a perspective might not be surprising, given that EOF analyses select spatial patterns that maximize global variance.

The results of this study show important differences between the NAO and PNA (Feldstein 2002). For example, it was found that the PNA life cycle was dominated by linear processes, in contrast to the nonlinear processes associated with the NAO (see subsection 5(b)). The results of Feldstein (2002) further suggested that the PNA could be interpreted simply as free, linear wave propagation in an inhomogeneous flow, implying

that the PNA can be understood from the viewpoint of an initial-value problem. This perspective about the PNA is further supported by the results of Cash and Lee (2001), who used a linear multivariate stochastic model to show that at least 70% of the observed PNA events evolve from the first optimal perturbation. This behaviour for the PNA strongly contrasts that for the NAO found in this study, where the NAO is interpreted as being a forced phenomenon.

The results of this study lead to further questions that need to be addressed in future studies. For example, what process excites the North Pacific wavetrain that precedes the onset of the positive NAO phase? What process organizes the North Atlantic transient eddies in such a manner so as to drive the NAO? What changes take place in the transient eddy structure that contribute to the NAO decay? What particular dynamical phenomena do the low-frequency transient eddies correspond to (this question is equally relevant for the PNA)? What role do baroclinic processes, e.g. eddy heat fluxes, diabatic heating, etc. play during the NAO life cycle? With regard to the latter question, a related issue is what processes drive the lower troposphere stream-function anomaly associated with the NAO? For this particular question, an analysis of the stream-function-tendency equation in the lower troposphere, e.g. 700 mb, may be ideal. It is anticipated that the lower-tropospheric stream-function anomaly associated with the NAO would result from anomalous divergence. This anomalous divergence would simply correspond to the secondary circulation that is induced by the upper tropospheric eddy driving. Lastly, there remains the basic question as to why the PNA and NAO are so different. A plausible answer involves the stronger stretching deformation field in the North Pacific and the enhanced storm-track variability in the North Atlantic. An investigation of each of the above issues is planned for in future research.

#### ACKNOWLEDGEMENTS

This research was supported by the National Science Foundation through Grant ATM-0003039. I would like to thank Drs Sukyoung Lee and Christian Franzke for their beneficial discussions. In addition, I would like to thank two anonymous reviewers for their very helpful comments on this paper, and also the National Oceanic and Atmospheric Administration Climate Diagnostics Center for providing me with the NCEP/NCAR re-analysis dataset.

#### REFERENCES

- |  |       |   |
|--|-------|---|
| Ambaum, M. H. P., Hoskins, B. J. and Stephenson, D. B. | 2001  | Arctic Oscillation or North Atlantic Oscillation? <i>J. Climate</i> , <b>14</b> , 3495–3507   |
| Barnston, A. G. and Livezey, R. E.                     | 1987  | Classification, seasonality, and persistence of low-frequency atmospheric circulation patterns. <i>Mon. Weather Rev.</i> , <b>115</b> , 1083–1126 |
| Cai, M. and van den Dool, H. M.                        | 1994  | Dynamical decomposition of low-frequency tendencies. <i>J. Atmos. Sci.</i> , <b>51</b> , 2086–2100  |
| Cash, B. A. and Lee, S.                                | 2001  | Observed nonmodal growth of the Pacific–North American teleconnection pattern. <i>J. Climate</i> , <b>14</b> , 1017–1028                          |
| Charney, J. G. and Drazin, P. G.                       | 1961  | Propagation of planetary scale disturbances from the lower into the upper atmosphere. <i>J. Geophys. Res.</i> , <b>66</b> , 83–109                |
| Deser, C.  | 2000  | On the teleconnectivity of the ‘Arctic Oscillation’. <i>Geophys. Res. Lett.</i> , <b>27</b> , 779–782   |
| DeWeaver, E. and Nigam, S.                             | 2000a | Do stationary waves drive the zonal-mean jet anomalies of the northern winter? <i>J. Climate</i> , <b>13</b> , 2160–2176                          |
|  | 2000b | Zonal-eddy dynamics of the North Atlantic Oscillation. <i>J. Climate</i> , <b>13</b> , 3893–3914  |
| Feldstein, S. B.                                       | 1998a | The growth and decay of low-frequency anomalies in a GCM. <i>J. Atmos. Sci.</i> , <b>55</b> , 415–428   |

- Feldstein, S. B. 1998b An observational study of the intraseasonal poleward propagation of zonal mean flow anomalies. *J. Atmos. Sci.*, **55**, 2516–2529
- 2000 The timescale, power spectra, and climate noise properties of teleconnection patterns. *J. Climate*, **13**, 4430–4440
- 2002 Fundamental mechanisms of the growth and decay of the PNA teleconnection pattern. *Q. J. R. Meteorol. Soc.*, **128**, 775–796
- Feldstein, S. B. and Lee, S. 1996 Mechanisms of zonal index variability in an aquaplanet GCM. *J. Atmos. Sci.*, **53**, 3541–3555
- 1998 Is the atmospheric zonal index driven by an eddy feedback? *J. Atmos. Sci.*, **55**, 3077–3086
- Franzke, C., Fraedrich, K. and Lunkeit, F. 2001 Teleconnection and low-frequency variability in idealized experiments with two storm tracks. *Q. J. R. Meteorol. Soc.*, **127**, 1321–1340
- Holton, J. R. 1992 *An introduction to dynamic meteorology*. Academic Press, San Diego, USA
- Honda, M., Nakamura, H., Ukita, J., Kousaka, I. and Takeuchi, K. 2001 Interannual seesaw between the Aleutian and Icelandic Lows. Part I. Seasonal dependence and life cycle. *J. Climate*, **14**, 1029–1042
- Honda, M. and Nakamura, H. 2001 Interannual seesaw between the Aleutian and Icelandic Lows. Part II. Its significance in the interannual variability over the wintertime northern hemisphere. *J. Climate*, **14**, 4512–4529
- Horel, J. D. 1985 Persistence of the 500 mb height field during northern hemisphere winter. *Mon. Weather Rev.*, **113**, 2030–2042
- Hurrell, J. W. 1995 Decadal trends in the North Atlantic Oscillation: Regional temperatures and precipitation. *Science*, **269**, 676–679
- Kushnir, Y. and Wallace, J. M. 1989 Low-frequency variability in the northern hemisphere winter: Geographical distribution, structure and time-scale dependence. *J. Atmos. Sci.*, **46**, 3122–3142
- Lee, S. and Feldstein, S. B. 1996 Mechanisms of zonal index evolution in a two-layer model. *J. Atmos. Sci.*, **53**, 2232–2246
- Livezey, R. E. and Chen, W. Y. 1983 Statistical field significance and its determination by Monte Carlo techniques. *Mon. Weather Rev.*, **115**, 46–59
- Lorenz, D. J. and Hartmann, D. L. 2001 Eddy–zonal flow feedback in the southern hemisphere. *J. Atmos. Sci.*, **58**, 3312–3327
- Mo, K. C. 1986 Quasi-stationary states in the southern hemisphere. *Mon. Weather Rev.*, **114**, 808–823
- Robinson, W. A. 1991 The dynamics of the zonal index in a simple model of the atmosphere. *Tellus*, **43A**, 295–305
- 1996 Does eddy feedback sustain variability in the zonal index? *J. Atmos. Sci.*, **53**, 3556–3569
- 2000 A baroclinic mechanism for the eddy feedback on the zonal index. *J. Atmos. Sci.*, **57**, 415–422
- Sardeshmukh, P. D. and Hoskins, B. J. 1988 The generation of global rotational flow by steady idealized tropical divergence. *J. Atmos. Sci.*, **45**, 1228–1251
- Thompson, D. W. J. and Wallace, J. M. 1998 The Arctic Oscillation signature in the wintertime geopotential height and temperature fields. *Geophys. Res. Lett.*, **25**, 1297–1300
- 2000 Annular modes in the extratropical circulation. Part I: Month-month variability. *J. Climate*, **13**, 1000–1016
- van Loon, H. and Rogers, J. C. 1978 The seesaw in winter temperatures between Greenland and Northern Europe. Part I: General description. *Mon. Weather Rev.*, **106**, 296–310
- Walker, G. T. and Bliss, E. W. 1932 World weather V. *Mem. R. Meteorol. Soc.*, **4**, 53–84
- Wallace, J. M. 2000 North Atlantic oscillation/annular mode: Two paradigms—one phenomenon. *Q. J. R. Meteorol. Soc.*, **126**, 791–805
- Wallace, J. M. and Gutzler, D. S. 1981 Teleconnections in the geopotential height field during the northern hemisphere winter. *Mon. Weather Rev.*, **109**, 784–812
- Yu, J. Y. and Hartmann, D. L. 1993 Zonal flow vacillation and eddy forcing in a simple GCM of the atmosphere. *J. Atmos. Sci.*, **50**, 3244–3259